Structure and lattice excitations of the copper substituted lead oxyapatite $Pb_{9.06(7)}Cu_{0.94(6)}(PO_{3.92(4)})_6O_{0.96(3)}$

Qiang Zhang ●,[1,*] Yingdong Guan,[2] Yongqiang Cheng,[1] Lujin Min,[2] Jong K. Keum,[1,3]
Zhiqiang Mao,[2] and Matthew B. Stone ●[1,†]

[1]*Neutron Scattering Division, Oak Ridge National Laboratory, Oak Ridge, Tennessee 37831, USA*
[2]*Department of Physics, Pennsylvania State University, University Park, Pennsylvania 16802, USA*
[3]*Center for Nanophase Materials Sciences, Oak Ridge National Laboratory, Oak Ridge, Tennessee 37831, USA*

The copper substituted lead oxyapatite, $Pb_{10-x}Cu_x(PO_{3.92(4)})_6O_{0.96(3)}$ [$x = 0.94(6)$] was studied using neutron and x-ray diffraction and neutron spectroscopy techniques. The crystal structure of the main phase of our sample, which has come to be colloquially known as LK-99, is verified to possess a hexagonal structure with space group $P6_3/m$, alongside the presence of impurity phases Cu and Cu_2S. We determine the primary substitution location of the Cu as the Pb1 (6h) site, with a small substitution at the Pb2 (4f) site. Consequently, no clear Cu-doping-induced structural distortion was observed in the investigated temperature region between 10 K and 300 K. Specially, we did not observe a reduction of coordinate number at the Pb2 site or a clear tilting of PO_4 tetrahedron. Magnetic characterization reveals a diamagnetic signal in the specimen, accompanied by a very weak ferromagnetic component at 2 K. No long-range magnetic order down to 10 K was detected by the neutron diffraction. Inelastic neutron scattering measurements did not show magnetic excitations for energies up to 350 meV. There is no sign of a superconducting resonance in the excitation spectrum of this material. The measured phonon density of states compares well with density functional theory calculations performed for the main LK-99 phase and its impurity phases. Our study may shed some insight into the role of the favored substitution site of copper in the absence of structural distortion and superconductivity in LK-99.

I. INTRODUCTION

Since claims of the observation of room-temperature superconductivity in a copper-substituted lead apatite compound emerged in 2023 [1], there was a rapid growth of interest in this compound. The parent compound, lead apatite $Pb_{10}(PO_4)_6O$ was proposed to become a superconductor with the substitution of copper as Cu^{2+} on the Pb^{2+} sites in the structure [2]. Spurred by this announcement, other researchers quickly attempted to reproduce the results. Synthesis of the compound, which has come to be colloquially known as LK-99, was found to be accompanied by an impurity phase of Cu_2S although no superconductivity was observed in subsequent magnetization measurements [3]. We note that this impurity phase was observed by the original group proposing superconductivity in this compound. Additional synthesis by other groups also observed the Cu_2S impurity phase along with electrical transport and magnetization measurements that are consistent with LK-99 being a semiconductor and not a superconductor [4]. It was argued that the first-order structural phase transition in Cu_2S is responsible for the signal in the magnetization, which was misinterpreted as superconductivity [5]. Growths of LK-99 with improved purity of precursor materials or single crystals were likewise unable to reproduce the proposed high-temperature superconducting phase [6,7].

Prompted by these experimental results, density functional theory (DFT) calculations of the parent compound and the copper substituted LK-99 have been performed by several groups [8–15]. Si and Held predicted an insulating electronic structure in the parent compound with a reduction in unit cell volume and flat bands near the Fermi energy appearing upon substituting Cu for Pb [8]. These flat bands imply a large electronic density of states near the Fermi level such that correlated electron behavior may be present in the material. Nonmagnetic DFT predicts the flat bands to have both hole and electron pockets while spin-polarized DFT calculations find that Cu substitution results in a ferromagnetic metal with $0.57\,\mu_B$ on the Cu site and a small hybridized moment of $0.06\,\mu_B$ on the nearest neighbor O site [9]. DFT calculations examining the lattice excitations of the Cu substituted compound have found that in a hexagonal structure, bands of phonons occur in the ranges 0 to 7, 11 to 13, 15 to 17, and 27 to 30 THz accompanied by an imaginary phonon mode, while in a triclinic lattice, the phonons have similar banding but without any imaginary modes [11].

Although room-temperature superconductivity in LK-99 has not been reproduced and its original observation is likely a misidentification due to a nonsuperconducting transition in an impurity phase, theoretical calculations do suggest the potential for correlated electron behavior. Such calculations rely heavily on details of the crystal structure and where the Cu sites are located in the substituted compound. Griffin *et al.* [15] predicted that the substitution of Cu on the Pb1 (4f) site induces a structural distortion and plays

*zhangq6@ornl.gov
†stonemb@ornl.gov

an important role in inducing key characteristics for high-T_C superconductivity, such as fluctuating magnetism, flat isolated d-manifold, charge, and phonons. This underscores the importance of investigating the substitution site of the copper, particularly considering the presence of two nonequivalent Pb sites in LK-99. In addition, as compared to x-ray diffraction, neutron diffraction is imperative for obtaining more precise information about oxygen positions and occupancy, which, unfortunately, has not been pursued. Here, in addition to the x-ray diffraction experiments, we conducted a series of neutron scattering measurements designed to better understand the nature of the crystal structure, investigate the lattice excitations, and probe for any indications of magnetic long-range order, magnetic fluctuations, or a superconducting resonance of LK-99.

II. EXPERIMENTAL AND THEORETICAL DETAILS

A. Sample preparation and magnetization measurements

We synthesized the $Pb_{10-x}Cu_x(PO_4)_6O$ compound following the procedures reported by Lee *et al.* [2]. High purity PbO and $PbSO_4$ powder were thoroughly mixed and loaded into an alumina crucible. The crucible was then heated to 725 °C and kept at this temperature for 24 hours in air. The product of $Pb_2(SO_4)O$ was verified by powder x-ray diffraction (XRD) analysis. Cu_3P was synthesized via heating the vacuum-sealed mixture of high-purity Cu and P powder. Our XRD measurements indicated that a tiny amount of Cu impurity remained in the Cu_3P product. $Pb_2(SO_4)O$ and Cu_3P were then mixed with a 1:1 molar ratio and sealed under vacuum in a quartz tube. The sealed tube was then heated to 925 °C and kept at this temperature for 15 hours. The formation of the $Pb_{10-x}Cu_x(PO_4)_6O$ phase was verified through Rietveld analysis on both XRD and neutron diffraction patterns. However, the product also contained impurity phases, including Cu and Cu_2S. Temperature and field dependence of the magnetization of the synthesized material was conducted using a commercial Superconducting Quantum Interference Device (SQUID, Quantum Design).

B. X-ray and neutron powder diffraction

XRD measurements were conducted on a PANalytical X'Pert Pro MPD equipped with an X'Celerator solid-state line detector at room temperature (RT). For the XRD measurements, the x-ray beam was generated at 45 kV/40 mA, and the x-ray beam wavelength was set at $\lambda = 1.5418$ Å (Cu Kα radiation). The step size ($\Delta 2\theta$) was 0.016° and the exposure time at each step was 200 seconds.

Neutron powder diffraction measurements were conducted at the time-of-flight neutron powder diffractometer POW-GEN, located at the Spallation Neutron Source (SNS) at Oak Ridge National Laboratory [16,17]. The POWGEN automatic changer (PAC) was used to collect data at temperatures $T = 10$ and $T = 300$ K. Approximately 0.5 grams of powder sample was sealed in a standard vanadium PAC can with helium exchange gas to ensure thermal contact with the PAC temperature stage. Two neutron detector banks with central neutron wavelengths of 0.8 Å and 2.665 Å were used to measure neutron powder diffraction over a wide range of *d* spacing.

To check the homogeneity of the sample and the substitution site of the Copper, the entire sample and two portions of the powder were subsequently used for XRD measurements at RT. The Rietveld analysis on XRD and neutron diffraction patterns was conducted using GSAS-II software [18].

C. Inelastic neutron scattering

Inelastic neutron scattering measurements were performed using the SEQUOIA instrument at the SNS at Oak Ridge National Laboratory [19,20]. The sample used was the same sample from the POWGEN measurements but sealed within a 6.35-mm diameter aluminum sample can in one atmosphere of helium gas to ensure good thermal contact with the sample environment cooling stage. Measurements were performed using the three-sample changer closed cycle refrigerator (CCR) environment at the spectrometer. An identical aluminum sample can was sealed and attached to the three-sample changer to provide a measurement of the empty-can scattering under the same instrument configurations as the sample measurements. Unless otherwise noted, presented data have had this empty-can scattering subtracted. Measurements were performed with the high-flux Fermi chopper set for incident energies of $E_i = 2000, 1000, 504, 249, 124, 59.4$, and 29.5 meV with frequencies of 600, 600, 480, 360, 240, 180, and 120 Hz. respectively. Measurements were also performed with the high-resolution Fermi chopper set for $E_i = 11.4$ meV at 180 Hz. All configurations were measured at $T = 5$ K with sample (empty-can) measurement counting times of 5(0), 5(2.5), 5(2.5), 5(2.5), 7.5(2.5), 9.23(3.87), 7.29(2.53), and 10(2.5) Coulombs of charge accumulated on the spallation target for the respective neutron energies listed above (from $E_i = 2000$ to 11.4 meV). Such longer counting times were used to account for the reduction in neutron flux at higher incident energies and the relatively small sample size. Some of these configurations were also measured at $T = 300$ K. The calculated full width at half maximum energy resolution for elastically scattered neutrons was $\delta\hbar\omega = 240, 86, 38, 18, 9.6, 4.3, 2.2$, and 0.24 meV for the incident energies of $E_i = 2000, 1000, 504, 249, 124, 59.4, 29.5$, and 11.4 meV respectively. Powder inelastic neutron scattering data are binned into intensity histograms as a function of scattering angle, 2θ, and energy transfer, $\hbar\omega$ using the inelastic algorithms in the MANTID software package [21]. Inelastic neutron scattering data are further binned as a function of the magnitude of wavevector transfer Q, and $\hbar\omega$ for presentation and analysis using DAVE software [22].

D. DFT calculations

Density functional theory (DFT) calculations of Cu, Cu_2S, and LK-99 were performed using the Vienna *Ab Initio* Simulation Package (VASP) [23]. The calculation used the Projector Augmented Wave (PAW) [24,25] method to describe the effects of core electrons, and Perdew-Burke-Ernzerhof (PBE) [26] implementation of the generalized gradient approximation (GGA) for the exchange-correlation functional. The spin-polarized calculation of LK-99 used the structure model and the Hubbard U (2.0 eV) as reported by Cabezas-Escares *et al.* [11]. Phonopy [27] and finite displacement method
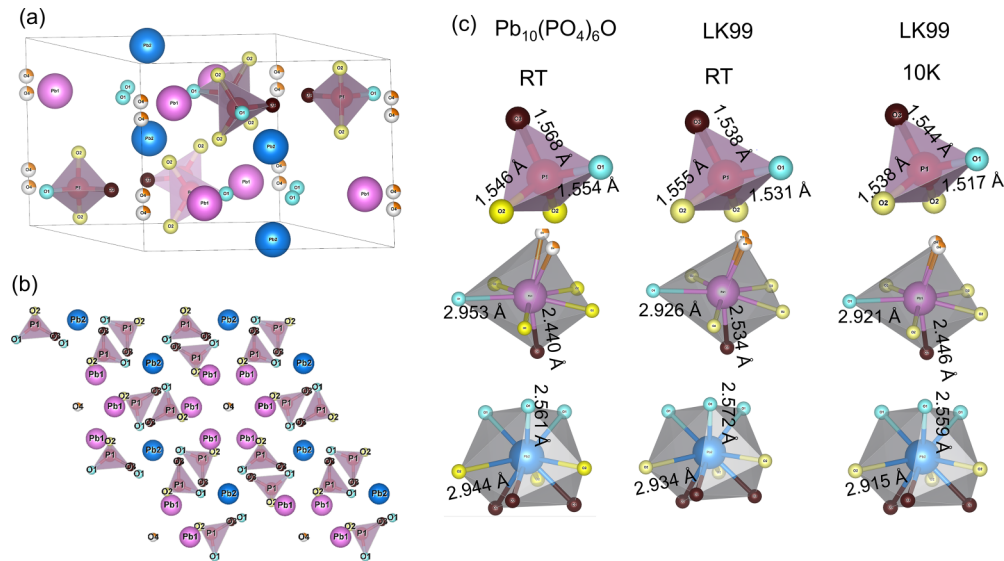
FIG. 1. (a) Three dimensional and (b) the projection of crystal structure in the *ab* plane of $Pb_{9.06(7)}Cu_{0.94(6)}(PO_{3.92(4)})_6O_{0.96(3)}$ obtained from the Rietveld analysis on the XRD and neutron powder diffraction data at 300 K. Copper primarily occupies the Pb1 (6*h*) site, with a small substitution at the Pb2 (4*f*) site. However, for the sake of simplicity, we utilize the same color for atoms in the display of Pb1 and Cu1 (or Pb2 and Cu2) atoms. (c) Comparison of the chemical environments of PO_4, $Pb1O_8$, and $Pb2O_9$ in the $Pb_{10}(PO_4)_6O$ at RT, Cu-doped LK-99 at RT and 10 K. The bond lengths of P-O in PO_4 tetrahedron and the longest/shortest Pb-O bond lengths have been added for comparison.

was used to obtain the interatomic force constants and subsequently the phonon frequencies and modes. The OCLIMAX [28] software was used to convert the DFT-calculated phonon results to the simulated INS spectra.

The structural model used for the DFT calculations is exactly the same as reported by Cabezas-Escares *et al.* [11]. The unit cell contains 1 Cu, 9 Pb, 6 P, and 25 O atoms, with the single Cu atom occupying the 4*f* site. While this does not fully match the composition and Cu arrangement observed in our structural refinement, we show that this simpler model properly accounts for most of the phonon features observed in the inelastic neutron scattering experiment. To account for the refined structure would require a much larger cell to describe the partial occupancies and disorder. Barring a fundamental change in the electronic structure, the relatively minor differences between the model used for the DFT calculation and the refined structure are unlikely to cause significant changes in the phonon density of states.

III. RESULTS AND DISCUSSION

A. Rietveld analysis of the crystal structure

To study the details of the crystal structure, we performed x-ray and neutron diffraction measurements on the same entire sample (≈ 0.5 grams). The determined crystal structure is displayed in Figs. 1(a) and 1(b). The XRD and neutron patterns at 300 K and the Rietveld co-refinement analysis of these patterns are shown in Figs. 2(a) and 2(b), respectively. In addition to the main LK-99 phase, there exist two impurity phases: Cu and Cu_2S. The crystal structure of Cu is cubic with space group *Fm-3m* (No. 225). Cu_2S crystallizes in a monoclinic structure with a space group $P2_1/c$ (No. 14), consistent with previous reports [3–5]. The weight fractions of LK-99, Cu, and Cu_2S are refined to be 41.2%, 24.1%, and
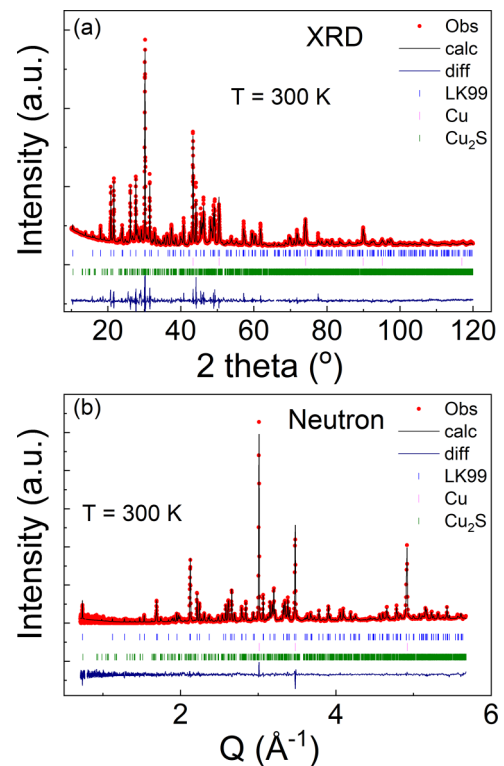

FIG. 2. Rietveld refinements of the (a) x-ray diffraction and (b) neutron powder diffraction patterns of $Pb_{9.06(7)}Cu_{0.94(6)}(PO_{3.92(4)})_6O_{0.96(3)}$ and its impurity phases at 300 K. The observed data and the fit are indicated by the open circles and solid lines, respectively. The difference curve is shown at the bottom. The vertical bars between the data and the difference curve mark the positions of Bragg reflections for the phases of LK-99 (upper ticks), impurity phases Cu (middle ticks) and Cu_2S (bottom ticks).

34.8%, respectively, based on the co-refinement on XRD and POWGEN patterns. Rietveld analysis reveals that we have synthesized the LK-99 phase that crystallizes in the hexagonal structure with space group $P6_3/m$ (No. 176). The lattice constants are refined to be $a = 9.839(7)$ Å, $c = 7.428(6)$ Å at $T = 300$ K, which are consistent with the initial reports by Lee et al. on LK-99 ($a = 9.843(4)$ Å, $c = 7.428(3)$ Å) [1,2]. The volume of the unit cell of our LK-99 sample is reduced by $\approx 0.56\%$ relative to the parent compound ($a = 9.8650$ Å, $c = 7.4306$ Å) [29], which is slightly larger than $\approx 0.48\%$ in the previous reports by Lee *et al.* [1,2] due to smaller lattice constant a. This indicates that Pb sites may be substituted by Cu and the smaller atomic radius of Cu than Pb is responsible for the shrinking of the unit cell. Note that our Rietveld analysis on both XRD and neutron data excluded superstructures with double c-axis parameter as reported for the parent compound $Pb_{10}(PO_4)_6O$ very recently [30].

Since the x-ray scattering cross-section is generally proportional to the atomic number Z, the x-ray scattering factor of Pb ($Z = 82$) is much larger than Cu ($Z = 29$). Consequently, x-ray diffraction proves to be a powerful tool to the determination of doping concentration of Cu on the Pb1 ($6h$) and/or Pb2 ($4f$) sites. Moreover, considering the larger neutron scattering length of Pb (9.405) in comparison to Cu (7.718), there exists an additional contrast that aids in elucidating the substitution sites of Cu by neutron diffraction. A careful Rietveld corefinement on both XRD and neutron patterns at 300 K has discerned that the doping concentration of Cu on Pb1 and Pb2 sites is 12.9(8)% and 3.9(6)%, respectively. This indicates that Cu is primarily substituted at the Pb1 ($6h$) site rather than the Pb2 ($4f$) site. Note that neutron data and XRD patterns co-refined were collected on the same 0.5 grams of powder sample in its entirety. To assess sample homogeneity and the substitution site of the copper, two additional XRD measurements were conducted on selected partial samples. The refinement on weight fractions unveiled a nonuniform distribution of LK-99, Cu, and Cu_2S within the sample. However, the weight fractions derived from the refinement of XRD and POWGEN patterns on the entire sample remained consistent. Notably, despite variations in weight fractions among the three samples, Rietveld analysis on their XRD patterns yields consistent doping concentrations of Cu on the Pb1 and Pb2 sites within the uncertainties for the main LK-99 phase. This finding aligns seamlessly with the Rietveld refinement results obtained from the POWGEN data, demonstrating a robust and coherent result. Furthermore, our findings corroborate theoretical calculations [15], illustrating that the replacement of Cu on the Pb1 ($6h$) site is energetically favored by 1.08 eV compared to the Pb2 ($4f$) site (Note that the labeling of Pb1 and Pb2 in this reference [15] is reversed with our labeling). In addition, we observed negligible vacancies at P, O1, O2, and O4 sites, whereas there is approximately a 7% vacancy at the O3 site. The refined composition of our sample is $Pb_{10-x}Cu_x(PO_{3.92(4)})_6O_{0.96(3)}$ [$x = 0.94(6)$], falling into the regime of the $0.9 < x < 1.1$ for the LK-99 in the previous reports [1,2].

It is instructive to compare the refined structural features between our LK-99 sample, the parent compound, and the prior theoretical calculations examining LK-99. In the parent compound $Pb_{10}(PO_4)_6O$ [29], three key polyhedra are

noteworthy: tetrahedra PO_4, $Pb1O_8$ and $Pb2O_9$ (with the cutoff 3 Å for the Pb-O bond length). Figure 1(c) displays the comparison of these polyhedra in the parent compound at RT, our LK-99 sample at RT and 10 K based on our Rietveld refinements. The theoretical predictions by Griffin *et al.* [15] suggest that the substitution of Cu on the Pb1 ($4f$) site, corresponding to the Pb2 ($4f$) site here, induces interesting structural distortion with two primary features. The first involves a reduction in coordination around the Pb2 ($4f$) site from nine to six, presenting a distorted trigonal prism coordination. The second entails a modification and tilting of the PO_4 tetrahedra. However, in our $Pb_{9.06(7)}Cu_{0.94(6)}(PO_{3.92(4)})_6O_{0.96(3)}$ compound, the coordination of Cu/Pb1 is maintained at 9 with the same Pb-O distance cutoff of 3 Å. For clarity, the longest and shortest Pb2-O bond lengths in $Pb2O_9$ have been included for the parent compound and our LK-99 in Fig. 1(c). No substantial changes in the Pb2-O bond lengths or clear distorted trigonal prism were observed due to Cu doping in our LK-99 compound. Furthermore, the coordination of Cu/Pb1 remains 8 using the same cutoff of 3 Å. The PO_4 tetrahedra in the parent compound does not form a regular tetrahedron since the O-P-O bond angle ranges from 106.4º to 111.9º, slightly deviating from the ideal angle 109.47º. In the $Pb_{9.06(7)}Cu_{0.94(6)}(PO_{3.92(4)})_6O_{0.96(3)}$ compound, we find that the O-P-O bond angle falls in the range from 106.23º to 111.6º, showing comparable bond angles relative to the parent compound at RT. Thus, no clear tetrahedral tilting is observed in the LK-99 compound. The P-O bond lengths were also incorporated in Fig. 1(c). Both parameters suggest that the Cu doping does not induce significant tilting of the PO_4 tetrahedron. Therefore, the predicted structural distortion [15] was not observed in our LK-99 compound.

It comes to our attention that Griffin *et al.* [15] predicted the structural distortion under the assumption that Cu substituted to the Pb2 ($4f$) site. However, our investigation reveals a minimal substitution ratio of Cu on the Pb2 ($4f$) site, with the majority of Cu predominantly entering the Pb1 ($6h$) site in the LK-99 sample. This finding may clarify why Cu doping does not induce the predicted structural distortion in the actual LK-99 sample. Furthermore, Griffin *et al.* [15] also predicted that the substitution of Cu on the Pb2 ($4f$) site plays a pivotal role in inducing key characteristics for high-T_C superconductivity, such as fluctuating magnetism, a flat isolated d-manifold, charge, and phonons. However, the predominant incorporation of Cu into the Pb1 ($6h$) site in the LK-99 sample, as opposed to the Pb2 ($4f$) site, may offer insights into the observed absence of room-temperature superconductivity in recent experiments [11]. The distinct distributions of Cu between the Pb1 and Pb2 sites necessitate a reevaluation in subsequent theoretical calculations.

B. Magnetic properties

The temperature dependence of the magnetization measured under zero-field-cooling (ZFC) and field-cooling (FC) histories in a field of 10 and 100 Oe is presented in Fig. 3(a). The magnetization is negative across the investigated temperature region 2–300 K, indicative of an overall diamagnetic response from the sample. Given that the impurity phases
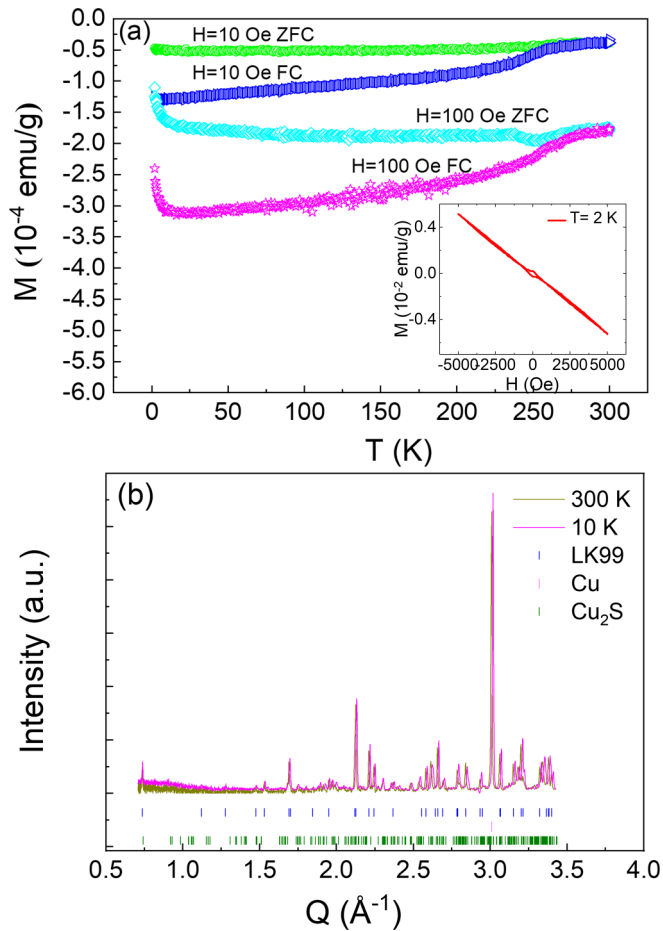
FIG. 3. (a) Temperature dependence of total magnetization after the ZFC and FC processes in a low field of 10 Oe and 100 Oe of the $Pb_{9.06(7)}Cu_{0.94(6)}(PO_{3.92(4)})_6O_{0.96(3)}$ with its impurity phases. The inset shows the magnetic hysteresis loop with field sweeping from +5000 to 0 to −5000 to 0 to 5000 Oe consecutively. (b) Comparison of low-Q POWGEN data between 300 K and 10 K showing the absence of any long-range magnetic order. The vertical bars between the data and the difference curve mark the positions of Bragg reflections for the phases of LK-99 (upper ticks), impurity phases Cu (middle ticks) and Cu_2S (bottom ticks).

Cu and Cu_2S are not diamagnetic in this temperature region, the diamagnetic behavior arises from the main LK-99 phase. This is consistent with observations in other polycrystalline compounds [2,3,5] or single crystal [7]. The upturn observed at low temperatures in an applied field of 100 Oe implies the existence of paramagnetic impurities, a phenomenon less prominent under an applied field of 10 Oe. Note that such an upturn is much weaker than those in the previous reports [2,5,7], indicating a lower fraction of paramagnetic impurities in our sample. The magnetic hysteresis loop, illustrated in the inset of Fig. 3 exhibits diamagnetic behavior. A small coercive field ≈ 400 Oe at 2 K indicates a very weak ferromagnetic component. This finding is consistent with observations in LK-99 single crystals [7], possibly arising from frustrated exchange interactions within the Cu-rich clusters.

The overplot of the POWGEN data in the low-Q region at 300 K and 10 K is displayed in Fig. 3(b). No discernible
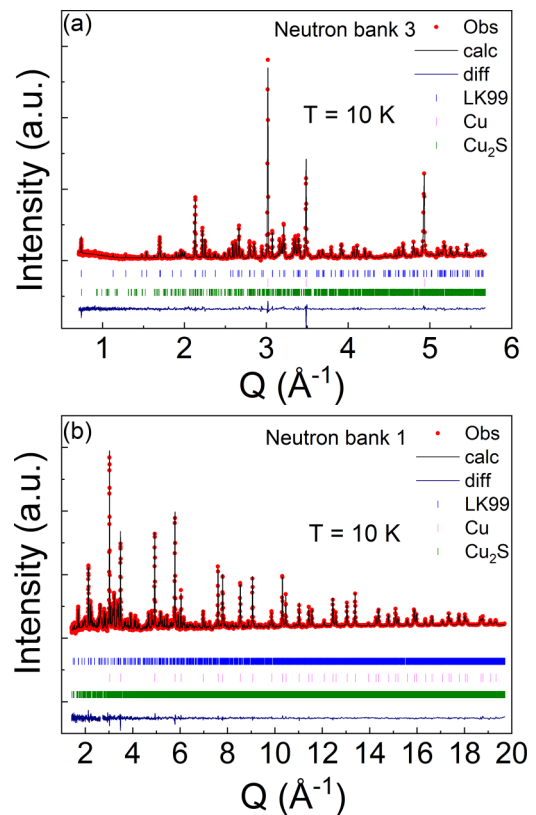

FIG. 4. Rietveld refinement fit to neutron powder diffraction patterns collected by (a) neutron bank 3 and (b) neutron bank 1 at the POWGEN instrument for $Pb_{9.06(7)}Cu_{0.94(6)}(PO_{3.92(4)})_6O_{0.96(3)}$ and its impurity phases at 10 K. The observed data and the fit are indicated by the open circles and solid lines, respectively. The difference curve is shown at the bottom. The vertical bars mark the positions of Bragg reflections for the phases of LK-99 (top), impurity phases Cu (middle), and Cu_2S (bottom).

pure magnetic peaks or an increase in peak intensity attributed to magnetic contributions were observed. Consequently, there is no indication of long-range magnetic order from 300 K down to 10 K in LK-99. The POWGEN data at 10 K can be well fitted using these three phases: LK-99, Cu, and Cu_2S, as shown in Figs. 4(a) and 4(b). Furthermore, there is no structural transition or clear structural distortion [see Fig. 1(c)] observed down to 10 K. The refined lattice constants, atomic positions, isotropic temperature factors and occupancy at 10 K are summarized in Table I.

C. Lattice excitations

Figure 5(a) shows the measured scattering intensity as a function of Q and $\hbar\omega$ for $E_i = 11.4$ meV neutrons measured at $T = 5$ K. There are no apparent magnetic fluctuations present in the spectrum. Figure 5(b) shows the integrated scattering intensity for elastically scattered neutrons with $-0.24 < \hbar\omega < 0.24$ meV. The reflections at $Q \approx 0.74$ and 1.1 Å^{-1} corresponding to d-spacings of ≈ 8.5 and 5.7 Å respectively, are in agreement with the 010 and 011 reflections observed in the POWGEN measurements. No additional Bragg reflections, beyond those measured at POWGEN, are discernible in the

TABLE I. Refined atomic positions, isotropic temperature factors, occupancy, from modeling high-resolution powder neutron diffraction data of $Pb_{9.06(7)}Cu_{0.94(6)}(PO_{3.92(4)})_6O_{0.96(3)}$ at 10 K. Analysis of the nuclear Bragg reflections lead to the space group selection of $P6_3/m$ (No. 176) and indexed unit cell constants of $a = b = 9.807(2)$ Å and $c = 7.399(8)$ Å. The refined composition is $Pb_{9.06(7)}Cu_{0.94(6)}(PO_{3.92(4)})_6O_{0.96(3)}$.

Atom	Site	x	y	z	U	occ
Pb1	6h	0.00210(5)	0.755(3)	0.25000	0.0070(5)	0.871(8)
Cu1	6h	0.00210(6)	0.755(6)	0.25000	0.0070(5)	0.129(8)
Pb2	4f	0.6667	0.3333	−0.00238(4)	0.0070(5)	0.961(6)
Cu2	4f	0.6667	0.3333	−0.00238(4)	0.0070(5)	0.039(6)
P1	6h	0.624(4)	0.597(6)	0.25000	0.0030(7)	1.021(7)
O1	6h	0.514(7)	0.664(6)	0.25000	0.0093(8)	1.032(7)
O2	12i	0.733(5)	0.651(2)	0.0842(7)	0.0093(8)	0.990(4)
O3	6h	0.530(6)	0.416(8)	0.25000	0.0093(8)	0.933(6))
O4	4e	0	0	0.215(8)	0.0093(8)	0.241(8)

inelastic measurements. Higher Q peaks are also structural and consistent with the POWGEN measurements.

Figure 6 shows the measured scattering intensity as a function of Q and $\hbar\omega$ for several incident energy measurements at both $T = 5$ and 300 K. For the $Ei = 504$, 249, 124, and 60 meV measurements, there is no significant scattering observed at lower values of wavevector transfer that would be consistent with magnetic scattering. The proposed
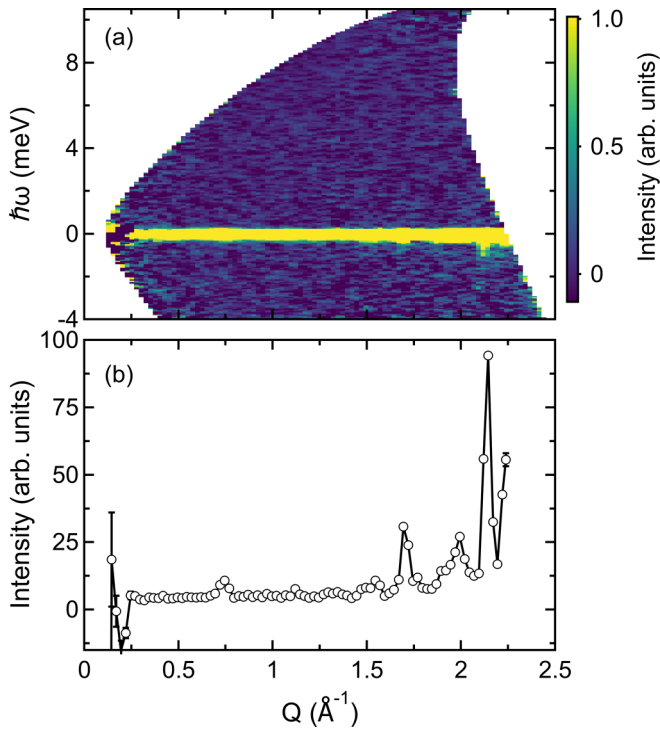

FIG. 5. Scattering intensity of $Pb_{9.06(7)}Cu_{0.94(6)}(PO_{3.92(4)})_6O_{0.96(3)}$ and its impurity phases at $T = 5$ K measured with $E_i = 11.4$ meV neutrons. Data have been background subtracted as described in the text. (a) Scattering intensity as a function of Q and $\hbar\omega$. (b) Scattering intensity for $-0.24 < \hbar\omega < 0.24$ meV as a function of Q.
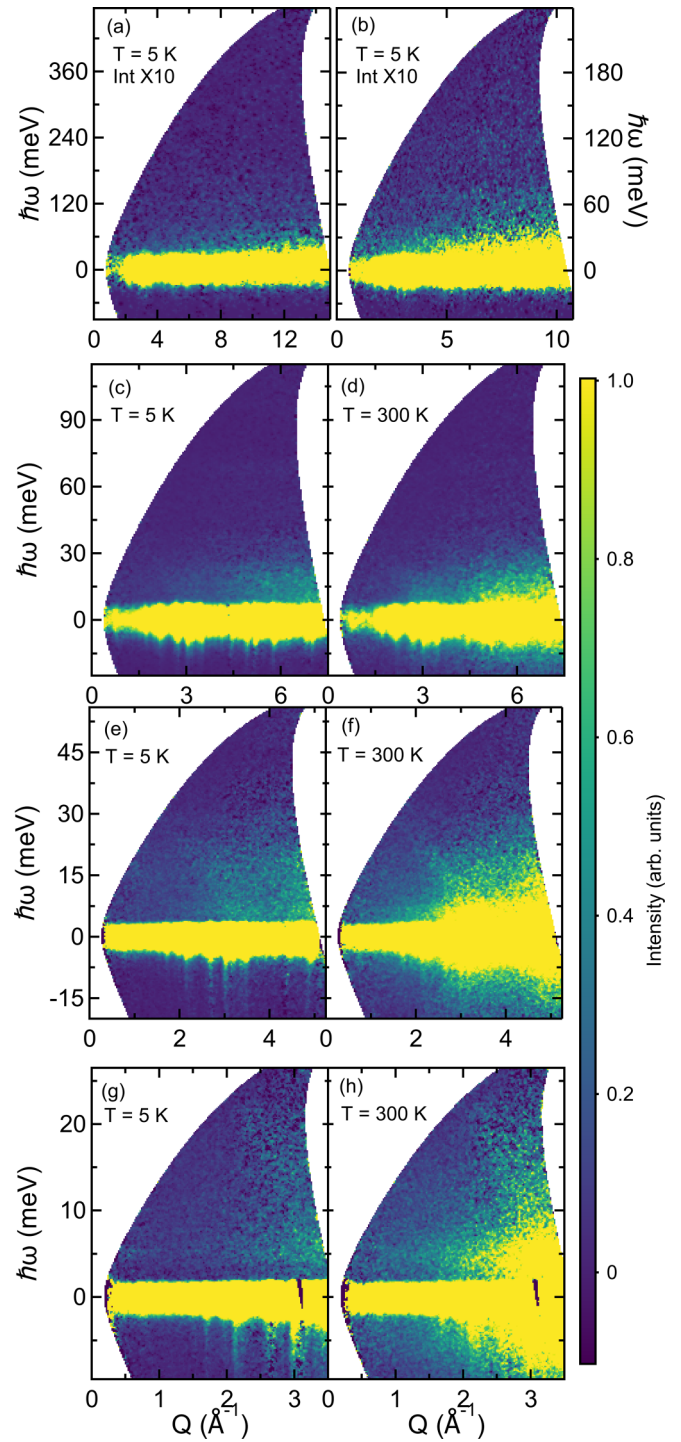

FIG. 6. Scattering intensity of $Pb_{9.06(7)}Cu_{0.94(6)}(PO_{3.92(4)})_6O_{0.96(3)}$ and its impurity phases at $T = 5$ K and $T = 300$ K as a function of Q and $\hbar\omega$ measured with different incident energy, E_i, neutrons. Data have been background subtracted as described in the text. (a) Scattering intensity for $Ei = 504$ meV and $T = 5$ K. (b) Scattering intensity for $Ei = 249$ meV and $T = 5$ K. (c)-(d) Scattering intensity for $Ei = 124$ meV and $T = 5$ K and $T = 300$ K respectively. (e)-(f) Scattering intensity for $Ei = 59.4$ meV and $T = 5$ K and $T = 300$ K respectively. (g)-(h) Scattering intensity for $Ei = 29.5$ meV and $T = 5$ K and $T = 300$ K respectively. The measured intensity shown in panels (a) and (b) is multiplied by a factor of 10.

superconducting transition temperature of $Pb_{10-x}Cu_x(PO_4)_6O$ was $T_C \approx 400$ K [1,2]. If LK-99 were an unconventional superconductor, one would expect potential superconducting resonances in the excitation spectrum [31]. Superconducting resonance energies E_r in inelastic neutron scattering measurements are observed at temperatures that are linearly proportional to the transition temperature. For example in the Fe-based superconducting compounds, this relationship has been found to be $E_r = 4.9k_BT_C$ [32], where K_B is Boltzmann's constant, and $E_r = 5.8k_BT_C$ for the cuprate superconductors [33]. Using the cuprate characteristic energy of the resonance for LK-99 would place the superconducting resonance at approximately 200 meV at low Q. No such feature is observed in our measured spectra. At larger values of wavevector transfer, a powder phonon density of states (PDOS) with bands of phonons extending up to $\hbar\omega \approx 120$ meV is observed.

The measured spectra for $E_i = 29.5$ meV have some scattering intensity appearing near $\hbar\omega = 6$ meV. This is present in both the $T = 5$ K and $T = 300$ K data as shown in Figs. 6(g) and 6(h), respectively. Figure 7 are plots of scattering intensity as a function of (a) Q and (b) and (c) $\hbar\omega$ for the $T = 5$ and 300 K measurements. The wavevector dependence, Fig. 7(a) is integrated between 4 and 7.5 meV and shows quadratic behavior for both temperatures consistent with this mode being associated with a lattice excitation. Intensity as a function of energy transfer for two different ranges of integration of wavevector transfer, Figs. 7(b) and 7(c), show that the $T = 5$ K mode has a peak in the vicinity of 5.5 meV, which softens slightly with increasing temperature and increases rapidly in intensity as a function of wavevector transfer making it further consistent with it being a lattice excitation.

We individually examine the generalized phonon density of states (PDOS) from the different incident energy neutron spectroscopy measurements. The scattering intensity was first plotted as a function of wavevector transfer for the $E_i = 29.5$, 59.4, and 124 meV configurations integrated over energy transfer ranges [4,8], [10,30], and [60,74] meV respectively. These data were individually compared as a function of energy transfer to the function $I(Q) = A + B * Q^2 \exp(-|u|^2Q^2)$ where A is an overall constant background, B is a multiplicative constant, and u quantifies the Debye-Waller factor. The mean Debye-Waller factor was then used with the DAVE software to extract the general phonon density of states for the $E_i = 29.5$, 59.4, 124, and 249 meV measurements for the integrated ranges of wavevector transfer [0.75,3.1],[2,4.5], [2.5,6.5], and [3, 8.5] Å^{-1} respectively [22]. The individual generalized phonon density of states is shown as a function of energy transfer for four different incident energies in Fig. 8. The variation in neutron flux as a function of incident energy was not applied as a normalization for these data. This accounts for the large variation in the magnitude of the density of states across the measurement configurations, which span an order of magnitude in neutron incident energy. Each measurement has characteristic features, which we enumerate as we discuss the analysis of these data.

DFT calculations of Cu, Cu_2S, and LK-99 were performed. The scattering intensity based upon the lattice excitation spectra calculated for the LK-99, Cu_2S, and Cu was convoluted individually with the instrumental energy resolution function for the $E_i = 29.5$ meV configuration. The three
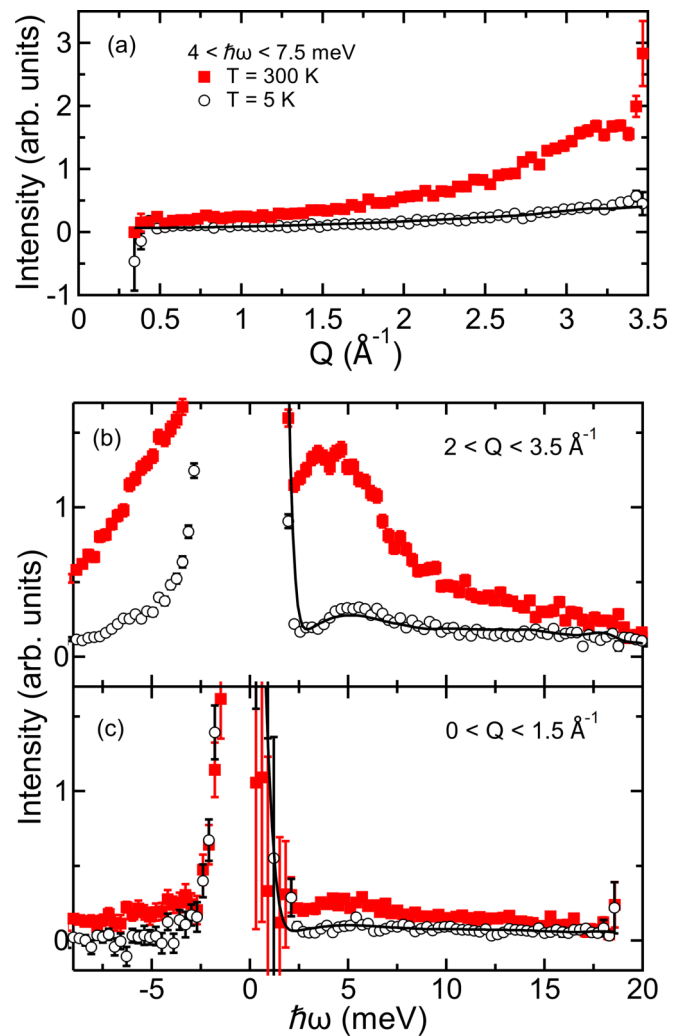

FIG. 7. Scattering intensity of $Pb_{9.06(7)}Cu_{0.94(6)}(PO_{3.92(4)})_6O_{0.96(3)}$ and its impurity phases at $T = 5$ K and $T = 300$ K for the $Ei = 29.5$ meV measurement. Data are cut through the spectra shown in Figs. 6(g) and 6(h) as a function of Q and $\hbar\omega$. Data have been background subtracted as described in the text. (a) Scattering intensities as a function of Q for energy transfers $4 < \hbar\omega < 7.5$ meV. (b) Scattering intensities for wavevectors $2 < Q < 3.5$ Å^{-1}. (c) Scattering intensities for wavevectors $0 < Q < 1.5$ Å^{-1}. Solid lines are fits to the $T = 5$ K data as the sum of scattering contributions from LK-99, Cu_2S, and Cu as described in the text. The range of the solid line along the independent variable indicates the range used for the fit of the data

spectra were added according to the percentages of each compound refined in analyzing the powder diffraction data. We fit the wavevector-dependent scattering intensity at low-energy transfer for the same cut through the data to this calculated resolution convolved scattering intensity, including an overall constant background and an overall multiplicative scaling factor. The result is shown in Fig. 7(a) as a solid line that reproduces the quadratic wavevector-dependent measured scattering intensity. We also fit separately the scattering intensity as a function of energy transfer using the same method for the data in Figs. 7(b) and 7(c). For this case, we include a Gaussian peak at zero-energy transfer to account for the
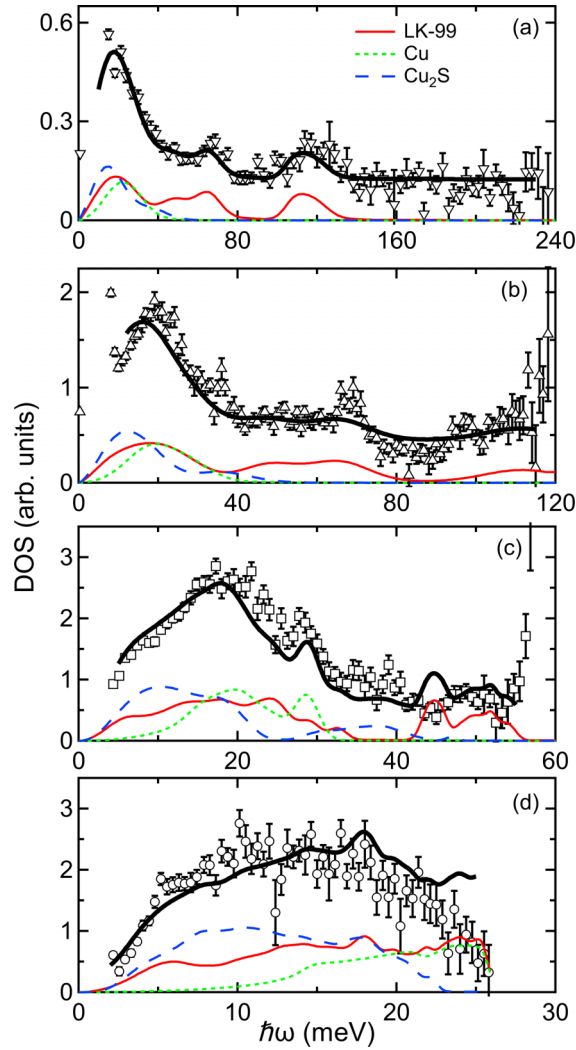
FIG. 8. Generalized phonon density of states for $Pb_{9.06(7)}Cu_{0.94(6)}(PO_{3.92(4)})_6O_{0.96(3)}$ and its impurity phases for $T = 5$ K. Data have been extracted into a general phonon density of states as described in the text. Data were acquired with four different incident energy configurations as described in the text: (a) $E_i = 249$ meV, (b) $E_i = 124$ meV, (c) $E_i = 59.4$ meV, and (d) $E_i = 29.5$ meV. The red solid lines are the calculated phonon density of states of $Pb_{9.06(7)}Cu_{0.94(6)}(PO_{3.92(4)})_6O_{0.96(3)}$ convolved with the respective energy transfer dependent resolution function for each of the measurement configurations as described in the text. The dashed blue and green dotted lines are similar calculations for Cu_2S and Cu, respectively, as described in the text. The heavy solid line is the refined combined phonon density of states that has been fit simultaneously to all of the measurements shown. This fit is further described in the text. The range used for the is the range of the black line. The individual phonon density of states is shown as their respective contribution to the overall measured phonon density of states but with no additional flat background included.

elastic scattering. The wavevector and energy transfer-dependent scattering intensity of the feature at approximately 5 meV energy transfer is well explained from the calculated lattice excitations of the LK-99 and its impurity phases.

We perform a similar fitting of the phonon density of states measurements shown in Fig. 8 to the calculated phonon

density of states convolved with the instrumental energy resolution. We fit simultaneously the four phonon spectra measurements shown in Fig. 8 to the sum of the calculated phonon density of states of LK-99, Cu_2S, and Cu with a fixed weighted percentage based upon the refined percentage of these compounds found in the analysis of the diffraction data. An overall constant background and a multiplicative scaling factor are also included for each of the incident energies in Fig. 8. The resulting fit to the phonon density of states is shown as a heavy solid line in the figure. The individual phonon density of states without the additive background is also shown in this figure separately for the three compounds. This fit provides an excellent representation of the measured density of states over more than two orders of magnitude of energy transfer. The bands of calculated phonons agree with calculations of phonon frequencies for LK-99 [11,34]. There is a larger relative background contribution in the phonon density of states at higher energy transfers. This is likely due to multiple scattering or multiphonon effects contributing to these higher energy transfers. Above $\hbar\omega \approx 40$ meV, the phonon density of states is dominated by the contribution from LK-99. The LK-99 modes in the vicinity of 70 meV are due to the O-P-O bending modes with motions deforming the PO_4 tetrahedra. The highest energy mode at approximately 110 meV is due to the stretching modes of the P-O bonds. One location with a difference in the calculated and measured phonon density of states is in the vicinity of $\hbar\omega = 44.6$ meV, Fig. 8(c). This mode corresponds to a twisting and scissoring type of motion resulting in squeezing of the PO_4 tetrahedra. The actual energy of this mode appears to be 4 meV higher at $\hbar\omega = 48.8$ meV. We speculate that this difference may be due to the relatively small unit cell used in the calculations.

Earlier, we considered where the superconducting resonance would occur in the spectrum if LK-99 were an unconventional superconductor. If LK-99 were a normal superconductor, electron-phonon coupling associated with the superconductivity would produce features in the excitation spectrum in the vicinity of the superconducting energy gap, 2Δ [35–37]. Considering a proposed transition temperature of $T_C \approx 400$ K and a range of plus or minus fifty percent deviation from weak, $2\Delta = 3.35 k_B T_C$, or strong, $2\Delta = 4 k_B T_C$ coupling limits results in a range between approximately 70 and 210 meV over which one would potentially see changes in the phonon spectrum [38]. We observe only modes that are consistent with the calculated phonon density of states in this energy range. All of the spectral features are well accounted for by the lattice excitations calculated for LK-99 and the Cu and Cu_2S impurity phases.

IV. CONCLUSIONS

We present a comprehensive analysis of the crystal structure, encompassing site occupancy, oxygen positions, and polyhedral environments, along with lattice excitations for the copper-substituted lead oxyapatite, $Pb_{10-x}Cu_x(PO_{3.92(4)})_6O_{0.96(3)}$ [$x = 0.94(6)$]. Our structural refinements reveal a favored substitution site of Copper on Pb1 (6*h*) site, which may provide insight into the absence of the Cu-doping-induced structural distortion and superconductivity in LK-99. Our DFT calculations for the

$Pb_{10-x}Cu_x(PO_4)_6O$, alongside impurity phases Cu and Cu_2S, predict a phonon spectrum entirely consistent with the measured spectrum. We find no experimental evidence of static long-range magnetic order, dynamic magnetic fluctuations, superconducting resonances, or superconductivity-correlated electron behavior in the LK-99.

[1] S. Lee, J.-H. Kim, and Y.-W. Kwon, The first room-temperature ambient-pressure superconductor, arXiv:2307.12008.

[2] S. Lee, J. Kim, H.-T. Kim, S. Im, S. An, and K. H. Auh, Superconductor $Pb_{10-x}Cu_x(PO_4)_6O$ showing levitation at room temperature and atmospheric pressure and mechanism, arXiv:2307.12037.

[3] K. Kumar, N. K. Karn, and V. P. S. Awana, Synthesis of possible room temperature superconductor LK-99: $Pb_9Cu(PO_4)_6O$, Supercond. Sci. Technol. **36**, 10LT02 (2023).

[4] L. Liu, Z. Meng, X. Wang, H. Chen, Z. Duan, X. Zhou, H. Yan, P. Qin, and Z. Liu, Semiconducting transport in $Pb_{10-x}Cu_x(PO_4)_6O$ sintered from Pb_2SO_5 and Cu_3P, Adv. Funct. Mater. **33**, 2308938 (2023).

[5] S. Zhu, W. Wu, Z. Li, and J. Luo, First-order transition in LK-99 containing Cu_2S, Matter **6**, 4401 (2023).

[6] K. Kumar, N. Kumar Karn, Y. Kumar, and V. Awana, Absence of superconductivity in LK-99 at ambient conditions, ACS Omega **8**, 41737 (2023).

[7] P. Puphal, M. Y. P. Akbar, M. Hepting, E. Goering, M. Isobe, A. A. Nugroho, and B. Keimer, Single crystal synthesis, structure, and magnetism of $Pb_{10-x}Cu_x(PO_4)_6O$, APL Mater. **11**, 101128 (2023).

[8] L. Si and K. Held, Electronic structure of the putative room-temperature superconductor $Pb_9Cu(PO_4)_6O$, Phys. Rev. B **108**, L121110 (2023).

[9] J. Lai, J. Li, P. Liu, Y. Sun, and X.-Q. Chen, First-principles study on the electronic structure of $Pb_{10-x}Cu_x(PO_4)_6O(x = 0,1)$, J. Mater. Sci. Technol. **171**, 66 (2024).

[10] R. Kurleto, S. Lany, D. Pashov, S. Acharya, M. van Schilfgaarde, and D. S. Dessau, Pb-apatite framework as a generator of novel flat-band CuO based physics, arXiv:2308.00698.

[11] J. Cabezas-Escares, N. F. Barrera, R. H. Lavroff, A. N. A. C. Cardenas, and F. Munoz, Theoretical insight on the LK-99 material, arXiv:2308.01135.

[12] S. Yang, G. Liu, and Y. Zhong, Ab initio investigations on the electronic properties and stability of Cu-substituted lead apatite (LK-99) family with different doping concentrations (x = 0, 1, 2), Mater. Today Communi. **37**, 107379 (2023).

[13] L. Si, M. Wallerberger, A. Smolyanyuk, S. di Cataldo, J. M. Tomczak, and K. Held, $Pb_{10-x}Cu_x(PO_4)_6O$: A Mott or charge transfer insulator in need of further doping for (super)conductivity, J. Phys.: Condens. Matter **36**, 065601 (2024).

[14] D. M. Korotin, D. Y. Novoselov, A. O. Shorikov, V. I. Anisimov, and A. R. Oganov, Electronic correlations in promising room-temperature superconductor $Pb_9Cu(PO_4)_6O$: A DFT+DMFT study, Phys. Rev. B **108**, L241111 (2023).

[15] S. M. Griffin, Origin of correlated isolated flat bands in copper-substituted lead phosphate apatite, arXiv:2307.16892.

[16] A. Huq, J. P. Hodges, O. Gourdon, and L. Heroux, Powgen: A third-generation highresolution high-throughput powder diffraction instrument at the spallation neutron source, in *European Powder Diffraction Conference; August 2010, Darmstadt, Germany* (Oldenbourg Wissenschaftsverlag, München, 2011), pp. 127–136.

[17] A. Huq, M. Kirkham, P. F. Peterson, J. P. Hodges, P. S. Whitfield, K. Page, T. Hugle, E. B. Iverson, A. Parizzi, and G. Rennich, POWGEN: Rebuild of a third-generation powder diffractometer at the Spallation Neutron Source, J. Appl. Crystallogr. **52**, 1189 (2019).

[18] B. H. Toby and R. B. Von Dreele, *GSAS-II*: the genesis of a modern open-source all purpose crystallography software package, J. Appl. Crystallogr. **46**, 544 (2013).

[19] G. E. Granroth, A. I. Kolesnikov, T. E. Sherline, J. P. Clancy, K. A. Ross, J. P. C. Ruff, B. D. Gaulin, and S. E. Nagler, SEQUOIA: A newly operating chopper spectrometer at the SNS, J. Phys.: Conf. Ser. **251**, 012058 (2010).

[20] M. B. Stone, J. L. Niedziela, D. L. Abernathy, L. DeBeer-Schmitt, G. Ehlers, O. Garlea, G. E. Granroth, M.

Graves-Brook, A. I. Kolesnikov, A. Podlesnyak, and B. Winn, A comparison of four direct geometry time-of-flight spectrometers at the spallation neutron source, Rev. Sci. Instrum. **85**, 045113 (2014).

[21] O. Arnold, J. Bilheux, J. Borreguero, A. Buts, S. Campbell, L. Chapon, M. Doucet, N. Draper, R. Ferraz Leal, M. Gigg *et al.*, Mantid—Data analysis and visualization package for neutron scattering and μSR experiments, Nucl. Instrum. Methods Phys. Res., Sect. A **764**, 156 (2014).

[22] R. T. Azuah, L. R. Kneller, Y. Qiu, A. Buts, P. L. Tregenna-Piggott, C. M. Brown, J. R. Copley, and R. M. Dimeo, Dave: A comprehensive software suite for the reduction, visualization, and analysis of low energy neutron spectroscopic data, J. Res. Natl. Inst. Stand. Technol. **114**, 341 (2009).

[23] Kresse, G. and Furthmüller, J., Efficient iterative schemes for *ab initio* total-energy calculations using a plane-wave basis set, Phys. Rev. B **54**, 11169 (1996).

[24] P. E. Blöchl, Projector augmented-wave method, Phys. Rev. B **50**, 17953 (1994).

[25] G. Kresse and D. Joubert, From ultrasoft pseudopotentials to the projector augmented-wave method, Phys. Rev. B **59**, 1758 (1999).

[26] J. P. Perdew, K. Burke, and M. Ernzerhof, Generalized gradient approximation made simple, Phys. Rev. Lett. **77**, 3865 (1996).

[27] A. Togo and I. Tanaka, First principles phonon calculations in materials science, Scr. Mater. **108**, 1 (2015).

[28] Y. Q. Cheng, L. L. Daemen, A. I. Kolesnikov, and A. J. Ramirez-Cuesta, Simulation of inelastic neutron scattering spectra using oclimax, J. Chem. Theory Comput. **15**, 1974 (2019).

[29] S. V. Krivovichev and P. C. Burns, Crystal chemistry of lead oxide phosphates: Crystal structures of $Pb_4O(PO_4)_2$, $Pb_8O_5(PO_4)_2$, and $Pb_{10}(PO_4)_6O$, Z. Kristallogr. Cryst. Mater. **218**, 357 (2003).

[30] S. V. Krivovichev and G. Engel, The crystal structure of $Pb_{10}(PO_4)_6O$ revisited: The evidence of superstructure, Crystals **13**, 1371 (2023).

[31] G. Yu, Y. Li, E. M. Motoyama, and M. Greven, A universal relationship between magnetic resonance and superconducting gap in unconventional superconductors, Nat. Phys. **5**, 873 (2009).

[32] W. Hong, L. Song, B. Liu, Z. Li, Z. Zeng, Y. Li, D. Wu, Q. Sui, T. Xie, S. Danilkin, H. Ghosh, A. Ghosh, J. Hu, L. Zhao, X. Zhou, X. Qiu, S. Li, and H. Luo, Neutron spin resonance in a quasi-two-dimensional iron-based superconductor, Phys. Rev. Lett. **125**, 117002 (2020).

[33] J. Zhao, P. Dai, S. Li, P. G. Freeman, Y. Onose, and Y. Tokura, Neutron-spin resonance in the optimally electron-doped superconductor $Nd_{1.85}Ce_{0.15}CuO_{4-\delta}$, Phys. Rev. Lett. **99**, 017001 (2007).

[34] Y. Jiang, S. B. Lee, J. Herzog-Arbeitman, J. Yu, X. Feng, H. Hu, D. Călugăru, P. S. Brodale, E. L. Gormley, M. G. Vergniory, C. Felser, S. Blanco-Canosa, C. H. Hendon, L. M. Schoop, and B. A. Bernevig, $pb_9Cu(PO_4)_6(OH)_2$: Phonon bands, localized flat-band magnetism, models, and chemical analysis, Phys. Rev. B **108**, 235127 (2023).

[35] J. D. Axe and G. Shirane, Influence of the superconducting energy gap on phonon linewidths in Nb_3Sn, Phys. Rev. Lett. **30**, 214 (1973).

[36] S. M. Shapiro, G. Shirane, and J. D. Axe, Measurements of the electron-phonon interaction in nb by inelastic neutron scattering, Phys. Rev. B **12**, 4899 (1975).

[37] F. Weber, A. Kreyssig, L. Pintschovius, R. Heid, W. Reichardt, D. Reznik, O. Stockert, and K. Hradil, Direct observation of the superconducting gap in phonon spectra, Phys. Rev. Lett. **101**, 237002 (2008).

[38] K. H. Bennemann and J. B. Ketterson, *Superconductivity* (Springer, Berlin, 2008).

[39] http://energy.gov/downloads/doe-public-access-plan.